

See discussions, stats, and author profiles for this publication at: <https://www.researchgate.net/publication/24036873>

X-ray Absorption Spectroscopy of VOCl_3 , CrO_2Cl_2 , and MnO_3Cl : An Experimental and Theoretical Study

ARTICLE in THE JOURNAL OF PHYSICAL CHEMISTRY A · MARCH 2009

Impact Factor: 2.69 · DOI: 10.1021/jp808720z · Source: PubMed

CITATIONS

12

READS

46

8 AUTHORS, INCLUDING:



Mauro Stener

Università degli Studi di Trieste

161 PUBLICATIONS 2,625 CITATIONS

SEE PROFILE



Monica De Simone

Italian National Research Council

108 PUBLICATIONS 936 CITATIONS

SEE PROFILE



Pietro Franceschi

Istituto Agrario di San Michele all'Adige (IA...)

61 PUBLICATIONS 544 CITATIONS

SEE PROFILE



Kevin Charles Prince

Sincrotrone Trieste S.C.p.A.

479 PUBLICATIONS 7,031 CITATIONS

SEE PROFILE

Article

**X-ray Absorption Spectroscopy of VOCl, CrOCl,
and MnOCl: An Experimental and Theoretical Study**

G. Fronzoni, M. Stener, P. Decleva, M. de Simone, M. Coreno, P. Franceschi, C. Furlani, and K. C. Prince

J. Phys. Chem. A, **2009**, 113 (12), 2914-2925 • DOI: 10.1021/jp808720z • Publication Date (Web): 24 February 2009

Downloaded from <http://pubs.acs.org> on May 5, 2009

More About This Article

Additional resources and features associated with this article are available within the HTML version:

- Supporting Information
- Access to high resolution figures
- Links to articles and content related to this article
- Copyright permission to reproduce figures and/or text from this article

[View the Full Text HTML](#)



ACS Publications
High quality. High impact.

The Journal of Physical Chemistry A is published by the American Chemical Society, 1155 Sixteenth Street N.W., Washington, DC 20036

X-ray Absorption Spectroscopy of VOCl_3 , CrO_2Cl_2 , and MnO_3Cl : An Experimental and Theoretical Study

G. Fronzoni,* M. Stener, and P. Decleva

Dipartimento di Scienze Chimiche, Università di Trieste, Via L. Giorgieri 1, 34127 Trieste, Italy, and Consorzio Interuniversitario Nazionale per la Scienza e Tecnologia dei Materiali, INSTM, Unità di Trieste, and INFN DEMOCRITOS National Simulation Center, Trieste, Italy

M. de Simone

CNR-INFN, Laboratorio Nazionale TASC, Trieste, Italy, and INSTM, Unità di Trieste

M. Coreno

CNR-IMIP, c/o Sincrotrone ELETTRA, Trieste, Italy, and INSTM, Unità di Trieste

P. Franceschi

Fondazione Edmund Mach, Centro Sperimentale IASMA, via E. Mach 1, 38010 San Michele all'Adige, Italy

C. Furlani

Dipartimento di Fisica, Università di Roma Tre e Accademia dei Lincei, Roma, Italy

K. C. Prince

Sincrotrone Trieste S.c.p.A, Trieste, Italy, and CNR-INFN, Laboratorio Nazionale TASC, Trieste, Italy

Received: October 2, 2008; Revised Manuscript Received: December 23, 2008

X-ray absorption spectra of gas-phase VOCl_3 and CrO_2Cl_2 have been measured in the metal $L_{2,3}$ -edge and O K-edge regions. The assignment of the spectral features is based on the relativistic two-component ZORA TDDFT approach. The calculations provide results in excellent agreement with the experimental spectra and prove the importance of including both configuration mixing and spin–orbit coupling in the theoretical description to obtain a reliable simulation of the transition metal $L_{2,3}$ -edge. The calculations are extended also to the MnO_3Cl molecule to discuss the spectral variations along the series of the oxychlorides both in the metal $L_{2,3}$ and ligand O K spectra.

1. Introduction

X-ray absorption spectroscopy (XAS) is a powerful tool for fundamental studies on isolated molecules as well as for the characterization of materials. The strength of XAS lies in its site specificity, tied to the possibility of selecting different core level edges of interest, and detailed information on the electronic and structural environment of a particular atomic element in a given compound can be obtained.

Experimental progress in the field of XAS has enabled the measurement of the transition metal (TM) $L_{2,3}$ absorption edges with great accuracy. The structures observed at the metal L edge in first row transition metal compounds involve $2p \rightarrow 3d$ electric-dipole transitions and the transition intensity directly reflects the amount of 3d metal character in the low-lying empty states. Similarly, the ligand K edge derives from a ligand centered $1s$ orbital, and only transitions to the ligand $2p$ component in the final state acquire intensity. Spin–orbit (SO) coupling plays an important role in the spectral shapes of L_3 and L_2 edges and influences their intensity distribution. When an electron is excited from a $2p$ core level to the virtual bound levels the spectrum consists of transitions to two closely related

manifolds of excited states, converging to the $2p_{3/2}$ (L_3) and $2p_{1/2}$ (L_2) thresholds, which are separated in energy by the SO splitting of the core hole. For 3d metal compounds the SO splitting varies from 5 to 20 eV and the L_3 edge is significantly different from the L_2 edge. Also the L_3/L_2 branching ratio is far from the ideal statistical value 2:1 expected from the ratio of the initial state degeneracy, as also observed in the case of pure 3d metals.¹ This behavior cannot be described within the one-particle theories, whose breakdown has been mainly ascribed to the interaction between the $2p$ core hole and the 3d excited electron.^{2–4} An approximation to account for this effect is to calculate the final state wave function in the presence of a hole in the core level involved in the absorption process. This approximation is included in several methods based on density functional theory (DFT) and implemented in computational codes which can simulate the single electron excitation of the X-ray absorption edge, such as the real-space-multiple-scattering code FEFF,⁵ the pseudopotential band structure WIEN2K code,⁶ as well as the quantum chemistry code as ADF.⁷ In the single particle model for excitations all other electrons do not participate in the spectroscopic transition; however, ignoring many-body effects other than the relaxation does not allow the reproduction of the experimental behavior of the L_3 and L_2 edge

* Corresponding author. E-mail: fronzoni@univ.trieste.it.

spectra of 3d metals.⁸ Fairly good agreement with experiment can be achieved by taking into account the 2p–3d two-particle interactions within a model based on atomic multiplet theory;² multiplet theory, including charge transfer and covalency effects, has become a de facto standard for the interpretation of L_3 - and L_2 -edge spectra in the solid state.^{1–3} In this approach, however, the treatment of orbital mixing due to molecular bond formation is simplified; furthermore a number of adjustable parameters are used. Approaches that go beyond the ground state and are significantly more time-consuming are based on the time-dependent density functional theory (TDDFT), which represents a rigorous extension of the DFT formalism for the treatment of the excited states or on the Bethe Salpeter equations.⁹

For free molecules, the recent formalism based on the relativistic two-component zero-order regular approximation (ZORA) and Time Dependent Density Functional theory (TD-DFT) extended to the treatment of the core electron excitations has been implemented in the ADF code.¹⁰ It represents a general and accurate theoretical approach capable of including both configuration mixing and SO coupling and appears of significant importance for a quantitative description and a reliable interpretation of the L-edge spectra of transition metal compounds. This method has been applied to the calculations of $L_{2,3}$ photoabsorption spectra of Ti in TiCl_4 ¹¹ and S in SO_2 ,¹² giving very satisfactory results. A somewhat similar approach to that developed by Zangwill and Soven for the simulation of the optical absorption of atoms and molecules¹³ has been recently presented,¹⁴ with the aim to describe the X-ray absorption in solids. In addition, this scheme is formulated in a fully relativistic way in order to describe the spin–orbit interaction, and its application to the $L_{2,3}$ absorption spectra of 3d transition metals demonstrates the importance of the core–hole interaction on the L_3/L_2 branching ratio. At the TDDFT level the mixing of the single 1h–1p (one hole–one particle) configurations allows the correlation effects between the 2p core hole and the 3d electrons to be described, as well as the coupling between different excitation channels which becomes allowed in the case of a degenerate core hole, such as 2p. This last effect plays an important role for a proper description of the L-edge of molecules¹⁵ and represents the many-body effect needed to improve the description of the intensity distribution among excited states converging to a single L-edge. The further inclusion of SO coupling in the computational scheme redistributes the calculated intensity over the two series of excited states converging to two different ionization thresholds $2p_{3/2}$ (L_3) and $2p_{1/2}$ (L_2). It is of interest to consider the potentiality of the TDDFT approach developed in the framework of the molecular orbital (MO) theory to the description of the $L_{2,3}$ absorption edges of an isolated molecule containing transition metals, for which high level electronic structure approaches can in principle describe with full accuracy the physical situation. Moreover MO theory provides a unified description of both degenerate (e.g., 2p) and nondegenerate (1s) holes, which are generally treated by different approaches, emphasizing the different dominant pictures in the two cases.

In this paper we present a theoretical and experimental study of the XAS spectroscopy of the series of oxychlorides VOCl_3 , CrO_2Cl_2 , and MnO_3Cl at the metal 2p and ligand O 1s thresholds. These are isoelectronic molecules in which the metal 3d orbitals are significantly involved in the bonding. Along the series the halogen atom is substituted stepwise with the oxygen atom as the number of d electrons increases in going from V to Mn, inducing variations in the L-edge spectra.

A complete set of absorption spectra is available at the 2p and 3p edges of the 3d metal atoms,¹⁶ and there is a wealth of data for solid compounds such as oxides, but high-resolution spectra at the $L_{2,3}$ -edges of several classes of transition metal compounds are still rare: for free molecules;^{17,18} for powders of transition metal complexes (with weak interaction between the metal centers),^{19,20} although some lower resolution EELS spectra of organometallic compounds are available;²¹ and also for clusters of transition metals.²² Also, few MO calculations of transition metal $L_{2,3}$ -edges are available including the SO contribution.^{11,23} In particular, for the oxychlorides the only previous calculations of the metal L-edges have been performed by using a nonrelativistic configuration interaction (CI) approach.¹⁸

The present high-resolution experimental spectra were measured by using a third-generation SR undulator beamline optimized to work in the VUV and a gas cell specifically built to perform absolute measurements of the photoionization cross section.¹⁸ The experiment makes possible both a clear identification of the excitation energies and a direct test of the theoretical approach for the calculation of the oscillator strengths. The experimental data presented are the $L_{2,3}$ -edge spectra of vanadium in VOCl_3 and of chromium in CrO_2Cl_2 . Moreover the O K-edge data are compared to new calculations. Both the SO splitting as well as the molecular field splitting are resolved in the present VOCl_3 and CrO_2Cl_2 experimental measurements resulting in significant complexity of the spectral features, so that the attribution of the core excited states can only be achieved with adequate theoretical support. At the V $L_{2,3}$ -edge an additional difficulty arises from the overlap among the structures relative to the V $L_{2,3}$ and O K absorption edges which fall in the same energy region. The calculation of the TDDFT spectrum at the O K core edge in VOCl_3 has allowed us to analyze in detail the origin of the peaks in this region. The MnO_3Cl molecule has been investigated only at the theoretical level. The O K edge spectra have been simulated for all the TM compounds at the same level of theory as for the $L_{2,3}$ metal edges, and the peak analysis has allowed us to discuss the degree of the metal–ligand bond covalency, since the intensity of the valence features can be related to the mixing among ligand and 3d metal orbitals. Furthermore, the direct comparison with the high-resolution experimental spectra for both the metal 2p and O 1s thresholds allows verification of the predictive power of the relativistic ZORA TDDFT method.

2. Theoretical Method

The core electron excitation spectra have been calculated by means of the relativistic two-component zeroth-order regular approximation (ZORA) and time-dependent density functional theory formalism,¹⁰ properly modified in order to treat core electron excitations. In this section we briefly recall the method, which is extensively described in ref 10.

This method allows the calculation of excitation energies and intensities for closed shell molecules, including spin–orbit coupling, and with full use of symmetry. The excitation spectrum is completely characterized by excitation energies ω_I and oscillator strengths $f_I = (4\pi^2/3)\alpha\omega_I|\langle\Psi_I|\hat{r}|\Psi_0\rangle|^2$. Employing a finite basis $\{\varphi_{i\sigma}\}$ the TDDFT equations are recast in the form of an eigenvalue equation:

$$\Omega F_I = \omega_I^2 F_I \quad (1)$$

$$\Omega_{ia\sigma,jb\tau} = \delta_{\sigma\tau}\delta_{ij}\delta_{ab}(\varepsilon_a - \varepsilon_i)^2 + 2\sqrt{(\varepsilon_a - \varepsilon_i)}\frac{\partial F_{ia}}{\partial P_{jb}}\sqrt{(\varepsilon_b - \varepsilon_j)} \quad (2)$$

in eq 2 indices i and j indicate occupied spinors and indices a and b indicate virtual spinors; ε_i and ε_a are molecular spinor energies, while F and P are the Fock matrix and density matrix, respectively.

In eq 1 the eigenvalues ω_l^2 correspond to the square of the excitation energies, while from the eigenvectors F_l the oscillator strengths can be extracted according to the standard TDDFT method.²⁴ The elements of the coupling matrix $\partial F_{ia}/\partial P_{ij}$ are calculated by means of the expression reported in ref 10, while eigenvalues and eigenvectors of the Ω matrix are obtained employing Davidson's iterative algorithm.²⁵

From the \bar{F}_l eigenvectors of eq 1 the intensity of the transition in terms of oscillator strengths can be easily calculated. In fact, following the treatment of Casida²⁴ it can be shown that the transition amplitudes \bar{F}_l are related to the x component of the transition moment between the ground state Ψ_0 and the excited state Ψ_l according to the following expression:

$$\bar{x}'S^{-1/2}\bar{F}_l = \omega_l^{1/2}\langle\Psi_0|\hat{x}|\Psi_l\rangle \quad (3)$$

where the transpose vector \bar{x}' corresponds to the dipole integrals between occupied-virtual molecular orbitals pairs:

$$x_{ij\sigma} = \int \phi_{i\sigma}\hat{x}\phi_{j\sigma} \, d\mathbf{r} \quad (4)$$

S is a diagonal matrix²⁴ and ω_l are the excitation energies. Therefore the oscillator strengths are finally obtained from the transition amplitudes \bar{F}_l with the following expression:

$$f_l = \frac{2}{3}(|\bar{x}'S^{-1/2}\bar{F}_l|^2 + |\bar{y}'S^{-1/2}\bar{F}_l|^2 + |\bar{z}'S^{-1/2}\bar{F}_l|^2) \quad (5)$$

A fundamental aspect of the implementation is the full use of molecular symmetry, which produces important computational economy if the molecule is highly symmetric. All the details of the double-group symmetry implementation with all the advantages such as block diagonal Ω matrix and reduction of numerical integrals to the symmetry-unique part of the integration grid by virtue of the Wigner–Eckart theorem are addressed in ref 10.

To treat the core electron excitations, the space spanned by the solutions of the eigenvalue eq 1, which corresponds to the 1h–1p excited configurations, is approximated by carefully selecting a subset of configurations, keeping only those necessary for an accurate description of the phenomenon, as is customary in ab initio CI calculations. In practice, the indices which span the occupied spinors (i and j) are limited to run over only the core shell under study, the two subshells 2p_{1/2} and 2p_{3/2} in the present case, thus allowing mixing of the initial states. Therefore, eq 1 is actually solved for a submatrix of the original Ω matrix, which is much smaller than the latter, and Davidson's algorithm can be effectively used because now core excitations correspond to the lowest states of the submatrix. With this approximation, the coupling between core excitations and valence excitations to the continuum is neglected and the computational scheme does not need the treatment of the continuum states. Moreover the coupling between core excitations and valence ionizations is expected to be very small

because similar schemes, employed in ab initio calculations,^{15,23} furnished excellent results with respect to the experiment. Scaled ZORA spinor eigenvalues are used in the calculations of core excitation energies.

2.1. Computational Details. The basis sets employed for the metal (V, Cr, and Mn), oxygen, and chlorine atoms are the all-electron ZORA basis sets for relativistic calculations from the ADF database named QZ4P (core triple- ζ , valence quadruple- ζ with 4 polarization functions).²⁶ These sets consist of STO functions and correspond to the [13s,8p,5d,3f] set for the metal atom, to the [11s,7p,3d,2f] set for the chlorine atom, and to the [8s,4p,2d,2f] set for the oxygen atom. The QZ4P ZORA basis set of the excited atom (metal in the 2p spectra and oxygen in the O K edge spectra) has been further augmented with two shells of s, p, d, and f diffuse functions, with exponents obtained with the even-tempered criterion ($\beta = 1.7$). Since the Rydberg excited states are involved, the inclusion of diffuse basis functions is necessary to describe the transitions to such states. The final basis sets for the excited atom are therefore the [15s,10p,7d,5f] set for the metal and the [10s,6p,4d,4f] set for oxygen. The adiabatic local density approximation (ALDA) was employed to approximate the exchange correlation (XC) kernel. For the XC potential applied in the Self Consistent Field (SCF) calculations the LB94²⁷ XC potential was used with the ground state electron configuration. The LB94 potential was chosen for its correct asymptotic behavior, which is a necessary condition for a good description of the high-energy valence virtual orbitals and Rydberg states. Its performance for the description of the core excitation spectra within the two-component ZORA TDDFT approach was tested in previous works.^{11,12} The experimental geometry was employed for all molecules except for MnO₃Cl; in this case the geometrical parameters of MnO₃F were assumed²⁸ and the Mn–Cl distance was set at 4.0 a_0 .

3. Experimental Section

The measurements were carried out on the undulator-based gas phase photoemission beamline at the Elettra synchrotron light source (Trieste, Italy²⁹), utilizing grating no. 5 covering the energy range 360–1000 eV. The photon energy was calibrated by using the center of the O 1s $\rightarrow \pi^*$ absorption band of CO at 534.21 eV.³⁰ The energy bandwidth used for measurements performed on VOCl₃ was better than 70 meV at the O K and V L_{2,3}-edge energies, while for those on CrO₂Cl₂ the bandwidth at the O K-edge was around 90 meV and that at the Cr L_{2,3}-edge was better than 110 meV. The lower photon resolution during these last measurements was due to the need to increase the signal-to-noise ratio, as the photon beam was suffering from instability at the time of the measurement.

The samples used were supplied by Aldrich (VOCl₃ 99.995% purity and CrO₂Cl₂ 99.99% purity). Care was taken in handling them to minimize contamination by moisture; in particular they were transferred to the sample holder in a glovebag filled with dry nitrogen. Both samples are liquid at room temperature, so they were subjected to several cycles of freezing and pumping in situ, to eliminate all traces of nitrogen and of others possible contaminants. Finally, the temperature was raised slowly and maintained at 295 K.

Vapors of the samples were introduced into the experimental chamber, consisting of a window-less double ionization chamber, equipped to record absolute total absorption cross section data of gas and vapors, described in our previous work.¹⁸ Absorption spectra of both substances were recorded at pressures between 6.0 and 9.6 $\times 10^{-3}$ mbar at room temperature.

As discussed previously,^{31,32} taking into account all the sources of errors (sample pressure, spectral bandwidth, higher

TABLE 1: Experimental and Calculated Excitation Energies (eV) and Oscillator Strengths f for the V $L_{2,3}$ Spectrum of VOCl_3 ^a

exptl		label	ΔE (eV) ^b	$10^2 f^c$	final state: ^d main config/ dominant character final MO
E (eV) ^b	$10^2 f (\pm 10\%)$				
−0.8 (2)	0.25	A ₀	−(0.52 ÷ 0.26)	weak transitions	$2a_{3/2}, 7e_{1/2} \rightarrow 13e$
(515.3)	0.94	A	(511.16)	0.397	$2a_{3/2} \rightarrow 13e/3d \text{ V}, 3p \text{ Cl}$
0.30	1.1		0.25	3.418	$2a_{3/2} \rightarrow 13e$
0.40	1.3				
1.10	0.79	B	0.88	0.060	$2a_{3/2} \rightarrow 14e/3d \text{ V}, 2p \text{ O}, 3p \text{ Cl}$
			1.62	1.714	$2a_{3/2} \rightarrow 14e$
1.60	6.9		1.67	7.308	$7e_{1/2} \rightarrow 14e$
			1.92	0.161	$7e_{1/2} \rightarrow 16a_1/3d \text{ V}, 2p \text{ O}, 3p \text{ Cl}$
2.70	11.3	C	2.46	6.213	$2a_{3/2} \rightarrow 16a_1$
3.20	2.4		2.89	6.696	$7e_{1/2} \rightarrow 16a_1$
		D	7.03	0.496	$6e_{1/2} \rightarrow 13e$
			7.10	0.189	$2a_{3/2} \rightarrow 15e/4s \text{ Cl}$
			7.23	3.662	$6e_{1/2} \rightarrow 13e$
		E	8.52	1.770	$6e_{1/2} \rightarrow 14e$
9.70			8.53	4.340	$6e_{1/2} \rightarrow 14e$
			8.74	0.579	$7e_{1/2} \rightarrow 21a_1/4s \text{ V}$
			8.89	0.409	$2a_{3/2} \rightarrow 18e/nd \text{ V} + 3d \text{ Cl}$
		F	9.38	1.404	$6e_{1/2} \rightarrow 16a_1 + 2a_{3/2} \rightarrow 19e/4p \text{ V} + nd \text{ V}$
			9.44	0.640	$7e_{1/2} \rightarrow 22a_1/ns \text{ V} + 6e_{1/2} \rightarrow 16a_1$
			9.63	3.714	$2a_{3/2} \rightarrow 20e/3d \text{ Cl} + nd \text{ V}$
			9.67	0.901	$7e_{1/2} \rightarrow 23a_1 + 6e_{1/2} \rightarrow 16a_1$
			9.87	1.712	$2a_{3/2} \rightarrow 23a_1/np, ns \text{ V}$
			9.99	3.287	$7e_{1/2} \rightarrow 23a_1 + 6e_{1/2} \rightarrow 16a_1$

^a Calculated two-component DFT-KS V 2p ionization limits are 521.78 eV ($2a_{3/2}$) and 521.75 eV ($7e_{1/2}$) (L_3 edge) and 528.94 eV ($6e_{1/2}$, L_2 edge), respectively. Experimental values: 524.85 eV ($2p_{3/2}$, L_3 edge), 532.55 eV ($2p_{1/2}$, L_2 edge). ^b The absolute excitation energy is given for the first intense line. Excitation energies relative to the first line are reported for the other transitions. ^c L_3 edge: only calculated transitions with $10^2 f > 0.100$ below the $2p_{3/2}$ ionization threshold (521.75 eV) are reported. L_2 edge: only transitions from $6e_{1/2}$ spinor ($2p_{1/2}$) are reported with $10^2 f > 0.0100$ up to the energy region of the F feature. ^d The initial MOs are characterized according to their double-group symmetry.

order light contamination) it is possible to estimate an error in the calculation of the integrated oscillator strength, which is below 10% in the case of VOCl_3 and below 20% in the case of CrO_2Cl_2 . Moreover, because we are always below 20 Mb in the absolute cross section, saturation effects are negligible in the present work.

3.1. Data Analysis. To compare the experimental absolute cross sections to the calculations of the oscillator strengths, we performed a Gaussian fit of the vanadium and chromium L_{3-} edges, with particular attention to the excitations below the $2p_{3/2}$ ionization threshold. The fits were performed on data plotted as $dI/dE [10^2 \text{ eV}^{-1}]$: in this way, the area of fitted peaks can be directly compared to the calculated oscillator strengths f corresponding to various final states. The use of Gaussian curves, instead of the Voigt function, is due to the choice to fit with one line a selected cluster of lines, as indicated in Tables 1 and 2, due to the large number of calculated excitation lines.

For the spectrum at the oxygen K-edge of CrO_2Cl_2 , we use the fit we already performed on the same data in a previous report.¹⁸ In particular, the fit was performed after the subtraction of a single arc tangent function centered at the ionization energy of O 1s,³³ to simulate the contribution due to excitation to the continuum. Unfortunately in VOCl_3 , the oxygen K-edge is just after the vanadium $L_{2,3}$ -edges, and for this reason we could not perform a reliable simulation of the background of this feature, so we simply removed a spline background to simulate the condition of zero oscillator strength before the discrete excitation region. Moreover, new theoretical calculations induced us to perform a new Gaussian fit by using a lower number of lines.

4. Results and Discussion

4.1. Metal $L_{2,3}$ Spectra. The calculated metal 2p excitation energies and oscillator strengths are reported in Tables 1–3

together with the experimental data; Figures 1–3 show the experimental and calculated spectra of VOCl_3 and CrO_2Cl_2 . The calculated excitation energies appear to be underestimated for both molecules with respect to the experiment, and this can be generally ascribed to deficiencies of the XC potential and to the self-interaction error typical of the Kohn–Sham scheme of DFT, which for core levels is much more pronounced than in the valence region. This is of no consequence on the relative energy scale, which represents the most important data for comparison with the experimental spectra; the experimental data have been accordingly shifted to the calculated ones in the figures. Figure 4 reports the theoretical spectrum of MnO_3Cl together with the theoretical spectra of VOCl_3 and CrO_2Cl_2 in order to discuss the spectral trend along the series with the splitting of the 3d metal orbital in the molecular field.

The MO scheme of the virtual valence levels, which are characterized by strong 3d metal contribution, is reported in Scheme 1 and can be useful to correlate the spectral features to the electronic structure of the molecules.

4.1.1. VOCl_3 . The experimental V $L_{2,3}$ -edge spectrum (Table 1 and Figures 1 and 3) shows three distinct regions of absorption: the lowest energy region is characterized by three distinct peaks, the central one by a broad and less resolved band, while a two-peaked structure is present around 530 eV (see Table 1), in the region of the O K-edge absorption. The first two structures are well separated in energy and correspond to the two spin–orbit components which converge to the vanadium L_3 ($2p_{3/2}$) and L_2 ($2p_{1/2}$) ionization thresholds. The last structure can be substantially assigned to the O 1s excitation, since the V $L_{2,3}$ -edge absorption is very low in this energy region according to the theoretical results.

Figure 3 shows the experimental deconvolution of the lowest energy region, which has been performed by using theoretical

TABLE 2: Experimental and Calculated Excitation Energies (eV) and Oscillator Strengths f for the Cr $L_{2,3}$ Spectrum of $\text{CrO}_2\text{Cl}_2^a$

exptl		label	ΔE (eV) ^b	$10^2 f^c$	final state: ^d main config/ dominant character final MO
E (eV) ^b	$10^2 f$ ($\pm 20\%$)				
(577.2) (2)	1.2	A	−(0.66 \div 0.15) (573.15)	weak transitions 0.914	$7e_{1/2}, 6e_{1/2} \rightarrow 17a_1, 4a_2$ $6e_{1/2} \rightarrow 17a_1/3d \text{ Cr}, 3p \text{ Cl}, 2p \text{ O}$
			0.28	0.995	$7e_{1/2} \rightarrow 4a_2/3d \text{ Cr}, 2p \text{ O}$
			0.31	0.187	$7e_{1/2} \rightarrow 11b_1/3d \text{ Cr}, 3p \text{ Cl}, 2p \text{ O}$
0.4	1.0		0.34	0.740	$6e_{1/2} \rightarrow 11b_1$
			0.41	0.462	$6e_{1/2} \rightarrow 11b_1 + 7e_{1/2} \rightarrow 4a_2$
0.8	1.1	B	0.88	1.911	$7e_{1/2} \rightarrow 11b_1$
1.1	1.4		1.06	2.471	$6e_{1/2} \rightarrow 11b_1$
1.4	1.5		1.33	0.102	$6e_{1/2} \rightarrow 18a_1/3d \text{ Cr}, 2p \text{ O}$
		C	1.74	0.739	$6e_{1/2} \rightarrow 18a_1 + 7e_{1/2} \rightarrow 18a_1$
1.8	1.1		1.89	1.196	$6e_{1/2} \rightarrow 9b_2/3d \text{ Cr}, 2p \text{ O}$
			2.02	0.225	$7e_{1/2} \rightarrow 9b_2$
2.1	3.7		2.13	5.040	$7e_{1/2} \rightarrow 18a_1$
2.7	5.5	D	2.88	5.300	$6e_{1/2} \rightarrow 9b_2$
3.1	4.5		2.97	7.475	$6e_{1/2} \rightarrow 9b_2 + 6e_{1/2} \rightarrow 18a_1$
		E	8.34	0.196	$5e_{1/2} \rightarrow 17a_1$
			8.54	1.084	$5e_{1/2} \rightarrow 17a_1$
			8.80	0.297	$7e_{1/2} \rightarrow 21a_1/nd \text{ Cr} + 5e_{1/2} \rightarrow 4a_2$
			8.84	0.286	$7e_{1/2} \rightarrow 11b_2/nd \text{ Cr} + 5e_{1/2} \rightarrow 4a_2$
			8.85	0.233	$7e_{1/2} \rightarrow 11b_2 + 5e_{1/2} \rightarrow 4a_2$
			8.88	0.356	$7e_{1/2} \rightarrow 21a_1 + 5e_{1/2} \rightarrow 4a_2$
			8.93	0.499	$6e_{1/2} \rightarrow 22a_1/nd \text{ Cr} + 5e_{1/2} \rightarrow 4a_2$
		F	9.31	0.469	$5e_{1/2} \rightarrow 11b_1$
			9.34	0.388	$7e_{1/2} \rightarrow 23a_1/4s \text{ Cr}, 4s \text{ Cl} + 5e_{1/2} \rightarrow 11b_1$
			9.44	0.291	$6e_{1/2} \rightarrow 12b_2/nd \text{ Cl}, np \text{ Cr}, nd \text{ Cr}$
			9.51	1.560	$5e_{1/2} \rightarrow 11b_1 + 7e_{1/2} \rightarrow 23a_1$
			9.52	1.140	$6e_{1/2} \rightarrow 12b_2 + 5e_{1/2} \rightarrow 11b_1$
			9.66	0.305	$6e_{1/2} \rightarrow 24a_1/4s \text{ Cr} + nd \text{ Cr}$
			9.69	0.214	$6e_{1/2} \rightarrow 14b_1/3d \text{ Cl}, nd \text{ Cr}$
			9.81	0.161	$7e_{1/2} \rightarrow 15b_1/3d \text{ Cl}, np \text{ Cr}, nd \text{ Cr}$
			9.83	0.128	$6e_{1/2} \rightarrow 15b_1$

^a Calculated two-component DFT-KS Cr 2p ionization limits are 584.42 eV ($6e_{1/2}$) and 584.39 eV ($7e_{1/2}$) (L_3 edge) and 593.13 eV ($5e_{1/2}$, L_2 edge), respectively. ^b The absolute excitation energy is given for the first intense line. Excitation energies relative to the first line are reported for the other transitions. ^c L_3 edge: only calculated transitions with $10^2 f > 0.100$ below the $2p_{3/2}$ ionization thresholds are reported. L_2 edge: only transitions from $5e_{1/2}$ spinor ($2p_{1/2}$) are reported with $10^2 f > 0.0100$, up to the energy region of the F feature. ^d The initial MOs are characterized according to their double-group symmetry.

data as a guide. In particular, to fit the first four structures of this region, we looked for the best fit using nine Gaussian curves corresponding to the calculated structures with oscillator strengths $10^2 f$ larger than 0.1. To reproduce the experimental spectrum well, we were obliged to include a rather weak peak before the first calculated band A (see Figure 1). A similar structure was observed also in the case of TiCl_4 ^{11,18} and we will discuss it later.

When comparing the two-component ZORA results for the V $L_{2,3}$ structure with the experimental spectrum (Figure 1), good agreement of the features is evident: the energy separation between the main features is correctly described and the intensity ratio is consistent with the experiment. The lack of a two-peak structure is evident in the theoretical V $L_{2,3}$ spectrum at higher energy; only weak absorption is present before the $2p_{1/2}$ threshold, therefore confirming the O K-edge origin of the experimental feature.

The main factors which influence the shape and the structure of the theoretical spectrum are the spin–orbit, multiplet, and molecular field splitting. The SO coupling splits the V $L_{2,3}$ core hole into the $2p_{3/2}$ and $2p_{1/2}$ levels; the C_{3v} symmetry of VOCl_3 removes the degeneracy of the $2p_{3/2}$ level, so that in the relativistic description, the 2p orbitals of vanadium correspond to the $2a_{3/2}$, $7e_{1/2}$ (L_3 components, split by only 0.03 eV), and $6e_{1/2}$ (L_2 component) spinors, each of them described as a

mixture of the $2e$ and $5a_1$ nonrelativistic components. The SO interaction leads to the series of spin–orbit partner states responsible for the appearance of the two main features converging to the L_3 - and L_2 -edges. The possible excited states contributing to L_3 structure can originate from both the $2a_{3/2}$ and $7e_{1/2}$ spinors and the total electronic wave function can have both A_1 and E symmetries. This explains the large number of lines calculated for the L_3 band among which the intensity redistributes. As concerns the molecular field effect on VOCl_3 , the C_{3v} symmetry splits the 3d shell into three virtual valence levels: the $13e$ (LUMO), $14e$, and $16a_1$ MOs, which are dominated by the V 3d component; contributions from O 2p and Cl 3p components are also present as a result of the V–ligand covalent interaction (see Scheme 1).

The molecular field is responsible for the splitting of the L_3 band into three major components, also present in the L_2 band, which are associated with the transitions from 2p core level to the three virtual valence MOs. The quality of the theoretical results can be assessed by comparison of the calculated L_2 – L_3 splitting (7.2 eV) and the experimental one (7.7 eV). Also the energy separation between the three components of the first band (1.42 and 1.00 eV) is in good agreement with the experimental values (1.20 and 1.10 eV).

We now consider in detail the theoretical results and the assignment of the spectral features. The V 2p excitations map

TABLE 3: Excitation Energies (eV) and Oscillator Strengths f for the Mn $L_{2,3}$ Spectrum of MnO_3Cl from Two-Component ZORA TDDFT Calculations^a

label	E (eV)	$10^2 f^b$	final state: ^c main config/ dominant character final MO
	637.7–637.9	weak transitions	$5e_{1/2}, 1a_{3/2} \rightarrow 10e$
A	638.35	2.214	$5e_{1/2} \rightarrow 10e/3d \text{ Cr}, 2p\text{O}$
	638.42	0.910	$1a_{3/2} \rightarrow 10e/3d \text{ Cr}, 2p\text{O}, 3p \text{ Cl}$
A'	638.95	1.186	$1a_{3/2} \rightarrow 15a_1/3d \text{ Cr}, 2p\text{O}, 3p \text{ Cl}$
B	639.62	3.399	$5e_{1/2} \rightarrow 15a_1 + 1a_{3/2} \rightarrow 11e/3d \text{ Cr}, 2p \text{ O}$
	639.81	0.541	$1a_{3/2} \rightarrow 11e + 5e_{1/2} \rightarrow 11e$
C	640.60	3.777	$5e_{1/2} \rightarrow 11e + 1a_{3/2} \rightarrow 11e$
	641.12	15.55	$5e_{1/2} \rightarrow 11e + 1a_{3/2} \rightarrow 11e$
D	648.68	2.282	$4e_{1/2} \rightarrow 10e$
	648.72	1.073	$4e_{1/2} \rightarrow 10e$
	648.99	0.187	$5e_{1/2} \rightarrow 15e/nd \text{ Mn}, 3d \text{ Cl}$
	649.02	0.187	$1a_{3/2} \rightarrow 15e + 1a_{3/2} \rightarrow 20a_1/ns \text{ Mn}$
	649.06	0.225	$1a_{3/2} \rightarrow 15e$
E	649.31	1.008	$4e_{1/2} \rightarrow 15a_1$
	649.74	2.581	$4e_{1/2} \rightarrow 15a_1$
	649.81	0.175	$5e_{1/2} \rightarrow 21a_1/np \text{ Mn}, ns \text{ Mn}$
	650.07	0.259	$5e_{1/2} \rightarrow 22a_1/ns \text{ Mn}$
	650.39	0.390	$5e_{1/2} \rightarrow 24a_1/nd \text{ Mn} + 1a_{3/2} \rightarrow 18e/np \text{ Mn}, nd \text{ Mn}$
F	650.77	1.250	$4e_{1/2} \rightarrow 11e$
	651–652		Rydberg transitions from $5e_{1/2}, 1a_{3/2}$ spinors (above $2p_{3/2}$ threshold)

^a Calculated two-component DFT-KS Mn 2p ionization limits are 650.32 eV ($5e_{1/2}$) and 650.37 eV ($1a_{3/2}$) (L_3 edge) and 660.20 eV ($4e_{1/2}$, L_2 edge), respectively. ^b L_3 edge: only calculated transitions with $10^2 f > 0.100$ below the $2p_{3/2}$ ionization threshold are reported. L_2 edge: only calculated transitions from $4e_{1/2}$ spinor ($2p_{1/2}$) with $10^2 f > 0.0100$ are reported up to the energy region of the F feature. ^c The initial MOs are characterized according to their double-group symmetry.

the V nd and V ns character of the final MOs; in the lower energy region the virtual valence MOs have predominant V 3d character so that significant intensity is calculated for these valence transitions. Peak A is assigned to the $2a_{3/2} \rightarrow 13e$ LUMO transitions, the main transitions of peak B are toward the second 14e valence level, and peak C derives from two excitations with similar intensity from the two $2a_{3/2}$ and $7e_{1/2}$ spinors to the third $16a_1$ valence level. In general we are led to attribute the energy splitting, as well as the different intensity distribution among states with dominant V 3d participation, to interference between energetically close excitations induced by configuration mixing. The A, B, and C calculated peaks describe correctly the shape of the valence experimental features, in particular the energy separation; only the intensity of the second peak is slightly overestimated with respect to the experiment, as is apparent from the comparison of the data in Table 1. The experimental spectrum shows a small peak about 1 eV lower than peak A (at 514.5 eV of absolute experimental energy). This peak is similar to the small leading peak found in the X-ray absorption spectra of d^0 compounds described with atomic multiplets, which is explained as an atomic multiplet line with a predominant triplet character.^{34,35} The present SO relativistic TDDFT scheme includes all the electronic states deriving from the spin-orbit coupling and the present calculations provide a series of weak lines (the total f value summed over the lines is 0.039) at the lower energy side of peak A, at around 510.7 eV. These are associated to transitions of the same nature as the more intense lines contributing to peak A, namely the $2a_{3/2} \rightarrow 13e$ LUMO

transitions. These lower energy excited states are not present in the spectrum calculated at the scalar relativistic level where the transitions to triplet states are forbidden, therefore they result from the spin-orbit coupling. The comparison with the A_0 prepeak in the experimental spectrum is, however, qualitative, for the very low intensity calculated for these transitions which also appear closer to peak A than in the experiment. In addition to a possible deficiency of the TDDFT Hamiltonian in describing the coupling strength of such states, other possible factors can contribute to the A_0 experimental peak, such as a quadrupole or a vibronic coupling allowed transition falling in this energy region.

The second band in the theoretical spectrum is dominated by three peaks (D, E, and F); the first two represent the L_2 components of the first two valence transitions: in fact, the main line of peak D corresponds to the $6e_{1/2} \rightarrow 13e$ LUMO transition while the two almost degenerate $6e_{1/2} \rightarrow 14e$ transitions give rise to peak E. Peak F has contributions from several lines: the first one is the $6e_{1/2} \rightarrow 16a_1$ transition, corresponding to the third valence $2p_{1/2}$ component, while the following states are expressed as a mixing of configurations involving also L_3 Rydberg transitions. Further intensity associated with the $6e_{1/2} \rightarrow 16a_1$ transition is therefore spread over several other excited states, as shown in Table 1. Other excitations contributing to peak F are due to transitions from the $2p_{3/2}$ core state to Rydberg levels converging to the L_3 edge, with V nd and ns character. Therefore the F peak consists of overlapping structures between the third valence excitation of the L_2 -edge and Rydberg transitions converging to the L_3 -edge. We underline that the molecular field splitting between the three valence excitations in the L_2 band (1.3 and 0.9 eV) closely reflects the splitting calculated for the L_3 components (1.4 and 1.0 eV). The higher energy side of the F peak (G and H structures in Figure 1) consists of a very large number of lines with low oscillator strength associated with transitions from the $2p_{3/2}$ core level ($2a_{3/2}$ and $7e_{1/2}$ spinors) to discrete states most of which fall above the L_3 -edge. The D, E, and F peaks are assigned to the experimental L_2 band, whose intensity appears quite large, although three possible less resolved peaks may contribute to it. The G and H theoretical features describe the higher energy tail of the L_3 experimental band. The following region (I, L, and M features) is characterized by a very low intensity and is assigned to Rydberg transitions from the $2p_{1/2}$ level ($6e_{1/2}$ spinor) which converge to the L_2 -edge. This result confirms that the two-peaked structure observed in the experiment in this energy range does not derive most of its intensity from V 2p excitations and is mainly composed of O 1s core excitations. The details of the calculated excitations contributing to G–M features can be found in Table S1 in the Supporting Information.

4.1.2. CrO_2Cl_2 . The experimental Cr $L_{2,3}$ spectrum (Figures 2 and 3) is characterized by two main features whose fine structure is less clearly resolved than in the V 2p spectrum, in particular for the higher energy structure. This is due to both a slightly lower resolution of the monochromator at this higher photon energy ($\Delta E = 110$ meV instead of 70 meV) and a poor quality photon beam during the acquisition, due to which the signal-to-noise level was worse than in case of V $L_{2,3}$. The large energy separation of the two main bands corresponding to the L_3 and L_2 SO components reflects the spin–orbit splitting of the Cr 2p initial states, which is 8.72 eV in the present calculations.^{32,33}

The agreement of the two-component ZORA Cr 2p results with the experimental spectrum is fairly good for both the energy separation between the two main features and the reproduction

SCHEME 1: Molecular Orbital Scheme of the Virtual Valence Levels of the DFT Ground State of VOCl_3 , CrO_2Cl_2 , and MnO_3Cl^a

VOCl_3 (C_{3v})		CrO_2Cl_2 (C_{2v})		MnO_3Cl (C_{3v})	
MO	$\Delta\epsilon$ (eV)	MO	$\Delta\epsilon$ (eV)	MO	$\Delta\epsilon$ (eV)
13e(LUMO) [3dV(58%), 3pCl(23%), 2pO(5%)]	(10.79)	17a ₁ (LUMO) [3dCr(40%), 3pCl(18%), 2pO(17%)]	(11.60)	10e (LUMO) [3dMn(42%), 2pO(46%), 3pCl(5%)]	(12.34)
14e	1.27	4a ₂ [3dCr(46%), 2pO(35%), 3pCl(6%)]	0.37	15a ₁ [3dMn(41%), 2pO(30%), 3pCl(24%)]	0.88
16a ₁ [3dV(48%), 2pO(27%), 3pCl(11%)]	2.37	11b ₁ [(3dCr(45%), 2pCl(23%), 2pO(18%)]	0.87	11e [3dMn(44%), 2pO(48%) 3pCl(1%)]	2.11
		18a ₁ [3dCr(45%), 2pO(33%), 3pCl(6%)]	1.92		
		9b ₂ [3dCr(44%), 2pO(38%), 3pCl(4%)]	2.54		

^a For each MO the following are reported: the main character in terms of atomic metal, chlorine and oxygen percentage contribution, and the energy separation $\Delta\epsilon$ from the LUMO KS energy value, which is taken as zero. (The absolute LUMO KS eigenvalues ($-\epsilon$) are reported in parentheses.)

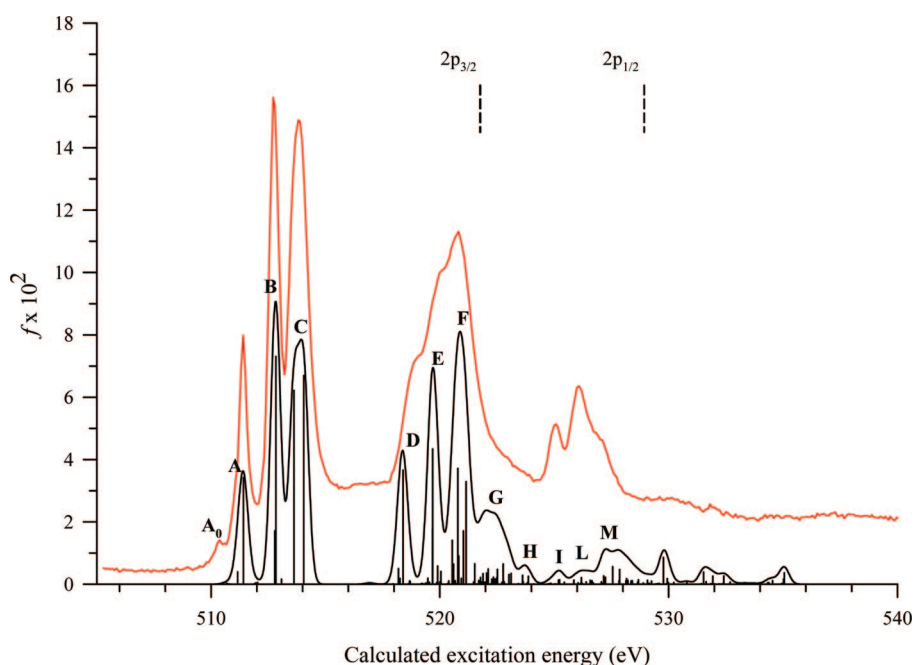


Figure 1. Vanadium $L_{2,3}$ spectrum of VOCl_3 . Black lines: two-component ZORA TDDFT spectrum. Vertical dashed lines: calculated vanadium $2p_{3/2}$ and $2p_{1/2}$ ionization limits. Convolved profiles are obtained with a Gaussian broadening of 0.5 eV of full width at half-maximum. Red line: experimental spectrum. The experimental profile has been shifted on the calculated energy scale (by 4.1 eV).

of the main components of the lowest energy L_3 band. The Gaussian profiles used for the convolution of the theoretical results describe the fine structure also for the higher energy band, useful to distinguish the excited states ascribed to the valence L_2 from Rydberg L_3 transitions. The intensity ratio among the calculated features is quite consistent with the experimental pattern, as can be verified from the data in Table 2.

It is again fruitful to consider both the molecular field splitting and the SO splitting to interpret the Cr 2p spectrum. Chromyl chloride has an approximately tetrahedral configuration, but the decrease of symmetry to C_{2v} causes a loss of degeneracy of the 3d shell, which splits into five virtual valence levels: the three lowest $17a_1$, $4a_2$, and $11b_1$ MOs, which roughly correlated to the 3-fold degenerate t_2 orbitals in T_d symmetry, and the remaining two $18a_1$ and $9b_2$ MOs, which could correspond to the e orbitals. The SO coupling splits the Cr 2p core hole into the $2p_{3/2}$ and $2p_{1/2}$ levels; in C_{2v} symmetry the $2p_{3/2}$ level is further split into the two almost degenerate $7e_{1/2}$ and $6e_{1/2}$ spinors (L_3 components, split by only 0.03 eV) and $5e_{1/2}$ (L_2 component)

spinors, each of them described as a mixing of the $2p_x$ (b_1), $2p_y$ (b_2), and $2p_z$ (a_1) nonrelativistic components. Transitions can start from each of the three 2p spinors to give rise to excited states of A_1 , B_1 , and B_2 dipole allowed symmetries of the total electronic wave function. The lowest energy L_3 band is assigned to the transitions starting from the $2p_{3/2}$ core hole to the virtual valence levels of mainly Cr 3d character. These virtual levels have contributions also from Cl 3p and O 2p components, and therefore represent the virtual counterparts of the Cr–ligand bonding MOs. The molecular field splitting is responsible for the fine structure of the L_3 band. Peaks A and B are due to transitions to the first three $17a_1$, $4a_2$, and $11b_1$ virtual valence MOs, while peaks C and D are associated with the two higher $18a_1$ and $9b_2$ MOs, respectively. A series of weak lines (the total f value summed over the lines is 0.258) are calculated at the lower energy side of peak A (around 573 eV), as in the previous V 2p spectrum. They describe the lower lying excited states (of A_1 , B_1 , and B_2 symmetry of the total wave function) relative to the transitions from the Cr 2p orbital to the $17a_1$ and

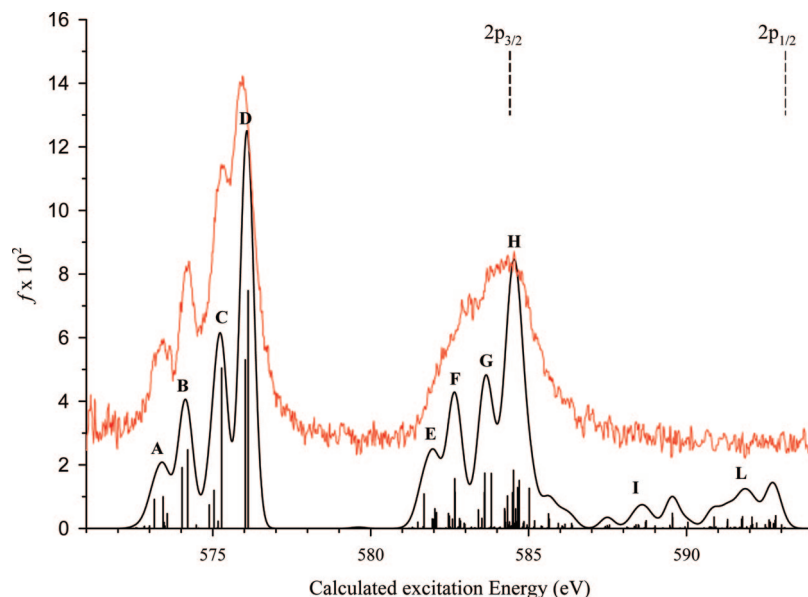


Figure 2. Chromium $L_{2,3}$ spectrum of CrO_2Cl_2 . Black lines: two-component ZORA TDDFT spectrum. Vertical dashed lines: calculated chromium $2p_{3/2}$ and $2p_{1/2}$ ionization limits. Convolved profiles are obtained with a Gaussian broadening of 0.5 eV of full width at half-maximum. Red line: experimental spectrum. The experimental profile has been shifted on the calculated energy scale (by 4.0 eV).

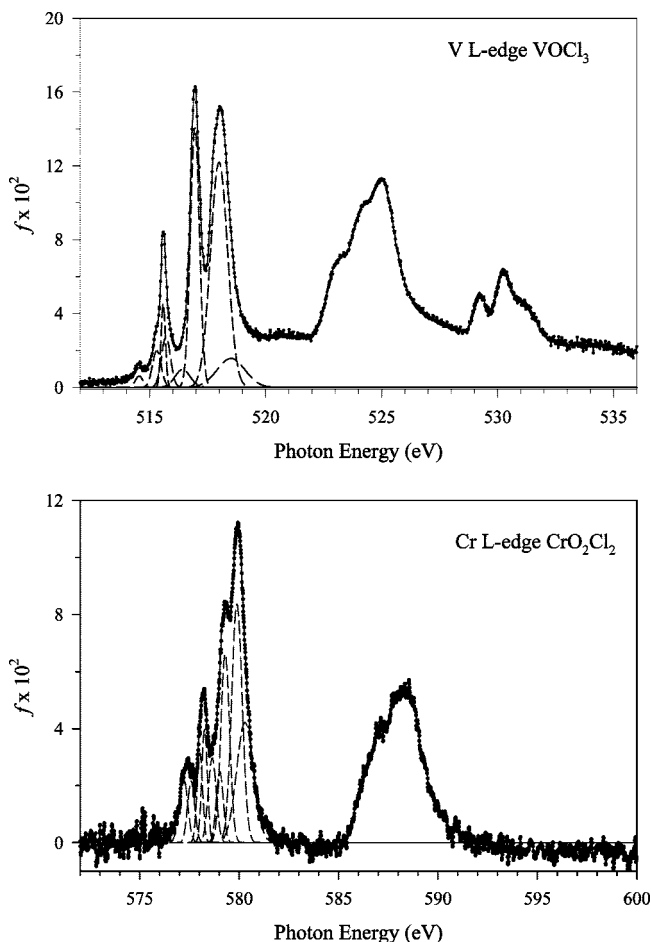


Figure 3. Experimental V and Cr $L_{2,3}$ spectra of VOCl_3 (upper panel) and CrO_2Cl_2 (lower panel). Dashed curves: Gaussian profile fit of the L_3 structure.

$4a_2$ virtual MOs. These calculated lines are hardly visible in Figure 2 and also in the experiment it is not possible to verify the possible presence of a prepeak due to the lower resolution than in the V2p experimental spectrum. The oscillator strength, which maps the Cr 3d participation in the final MOs, increases

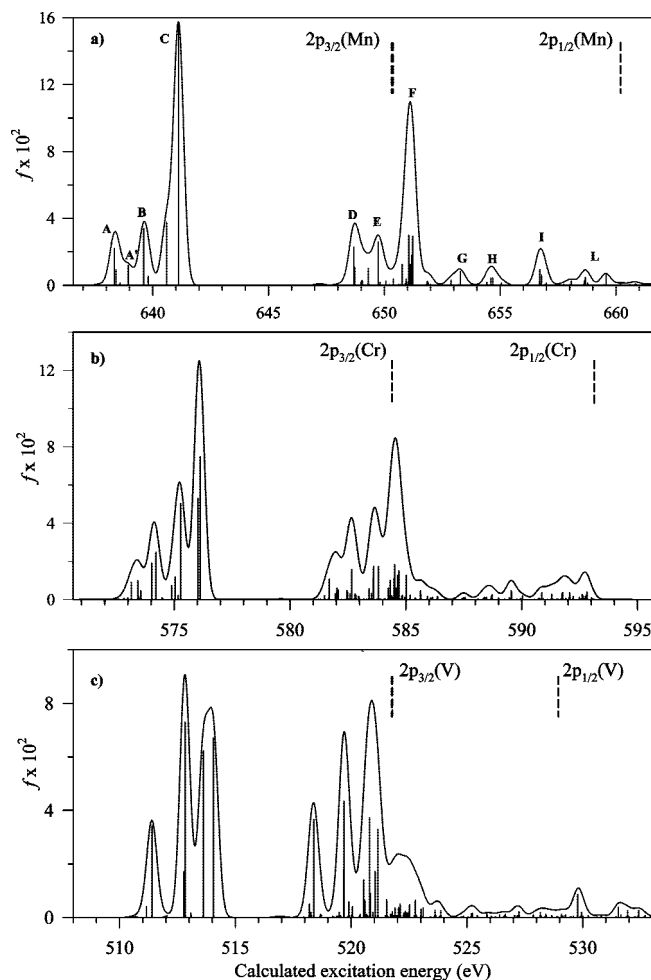


Figure 4. Metal $L_{2,3}$ two-component ZORA TDDFT spectra of MnO_3Cl , CrO_2Cl_2 , and VOCl_3 . Vertical dashed lines: calculated metal $2p_{3/2}$ and $2p_{1/2}$ ionization limits. Convolved profiles are obtained with a Gaussian broadening of 0.5 eV of full width at half-maximum.

on going from peak A to D, due to the decrease of the p ligand components and of the parallel shift of Cr 3d contribution to

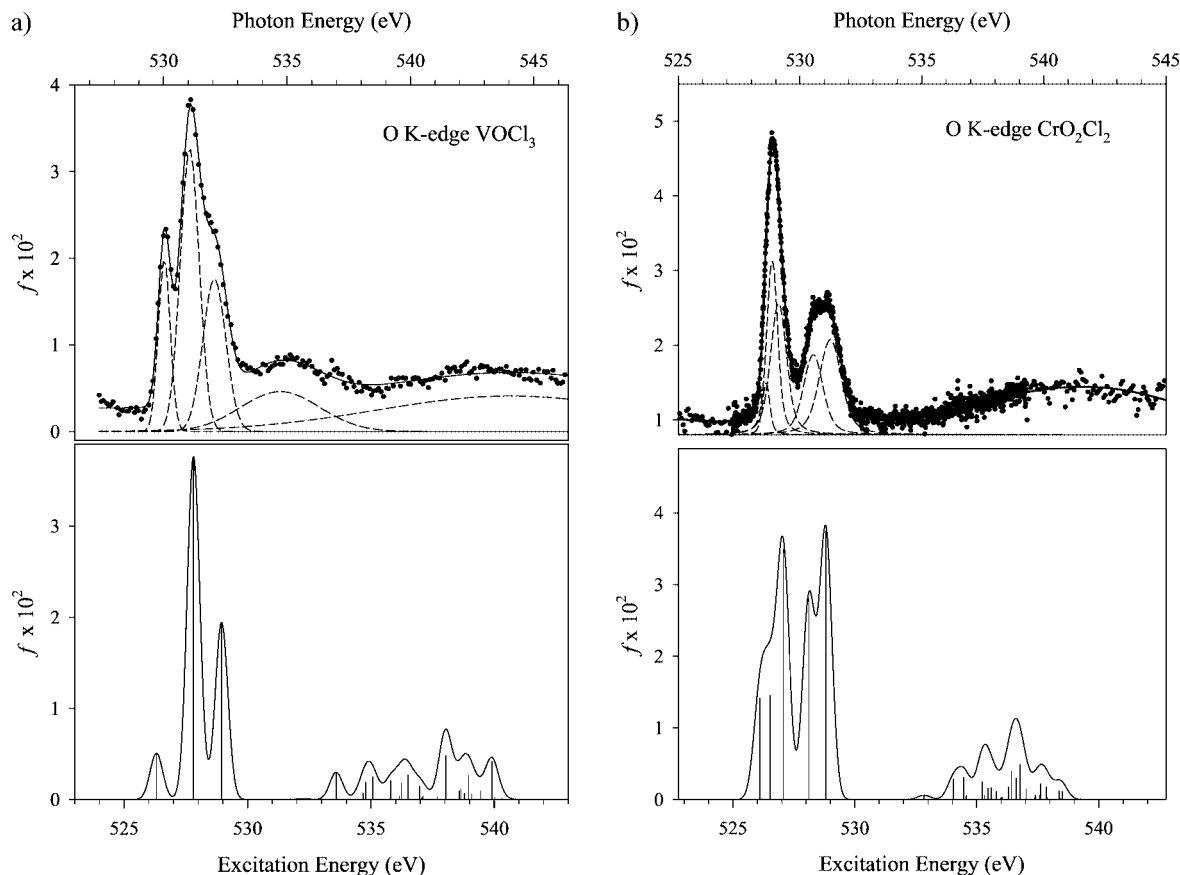


Figure 5. O K-edge spectra of VOCl_3 (panel a) and CrO_2Cl_2 (panel b). Upper panels: points, experimental result; full line, the fit results; dashed lines, fitted Gaussian curves. Lower panels: calculated spectra.

the upper levels of the virtual valence manifold. The four theoretical peaks describe correctly the four features resolved in the experiment both as concerns the energy separation and the intensity trend. The agreement between the theoretical and experimental oscillator strength of the single features is not quantitative (see Table 2), with a general overestimation of the calculated with respect to the experimental values.

The convolution of the theoretical lines calculated above 580 eV reveals four main peaks also for the second feature of the calculated spectrum. Peak E mainly consists of transitions from the $5e_{1/2}$ spinor to $17a_1$ and $4a_2$ final state MOs, and therefore corresponds to the $2p_{1/2}$ SO component of peak A; analogously, the most intense excitations of peak F ($5e_{1/2} \rightarrow 11b_1$) correspond to the SO partner states of peak B, although several transitions from the $2p_{3/2}$ core hole to Rydberg states of Cr *ns* and *nd* character appear in this energy region. We underline that several excited states in this energy region are expressed as a mixing of configurations, which is responsible for a spread of the intensity over a large number of lines. The overlap of Rydberg transitions converging to the $2p_{3/2}$ edge and valence transitions starting from the $2p_{1/2}$ core hole is more noticeable on going toward higher energy; the remaining SO partner virtual valence states ($5e_{1/2} \rightarrow 18a_1$ and $9b_2$ transitions) both contribute to peak G and only to a lesser extent to peak H. This last peak mainly derives from higher Rydberg excitations converging to the $2p_{3/2}$ ionization threshold. Therefore the second experimental band can be assigned to $2p_{1/2}$ (L_2) valence transitions overlapping a large number of less intense Rydberg L_3 transitions. In the region labeled I are present transitions from the $2p_{3/2}$ spinors into virtual MOs falling above the L_3 -edge while the Rydberg excitations from the $2p_{1/2}$ core hole start at about 588 eV and give rise to the featureless structure labeled L at the higher

energy side of the calculated spectrum. The details of the calculated excitations contributing to G–L features can be found in Table S2 in the Supporting Information.

4.1.3. MnO_3Cl and Comparison of the Metal $L_{2,3}$ Theoretical Spectra. Only the theoretical spectrum is available for the MnO_3Cl molecule. The results are shown in Table 3 and Figure 4 (panel a). The figure also reports the theoretical Cr 2p and V 2p spectra (panels b and c) in order to compare and discuss the spectral trends along the series. We consider first the results for MnO_3Cl . The Mn $2p_{3/2}$ and $2p_{1/2}$ SO coupled levels are split into $5e_{1/2}$ and $1a_{3/2}$ (L_3 components, separated by 0.05 eV) and $4e_{1/2}$ (L_2 component) spinors. The molecular field also splits the Mn 3d shell into three virtual valence levels, 10e (LUMO), $15a_1$, and $11e$ MOs, which have mainly 3d metal character with contributions also from O 2p and minor Cl 3p components. The MnO_3Cl spectrum is again characterized by the presence of two main features: a lower energy band due to a few transitions from the $2p_{3/2}$ core hole to the virtual valence levels, and a more complex structure extending around the $2p_{3/2}$ ionization threshold up to the L_2 edge, which derives from a large number of excitations. Both A_1 and E symmetries of the total electronic wave function are dipole allowed for transitions starting from each of the three 2p spinors. The molecular field splitting is responsible for the three major components of the lowest energy structure which correspond to transitions from the Mn $2p_{3/2}$ core level to the three virtual valence MOs (L_3 band). In particular, peak A is attributed to the $2p_{3/2} \rightarrow 10e$ transitions, the shoulder A' at the higher energy side of peak A and the peak B correspond to the $15a_1$ transitions while peak C corresponds to the $11e$ transitions (see Table 3). Also for the Mn 2p spectrum the calculations provide a series of weak lines at the lower energy side of peak A (at around 637.8 eV), which correspond

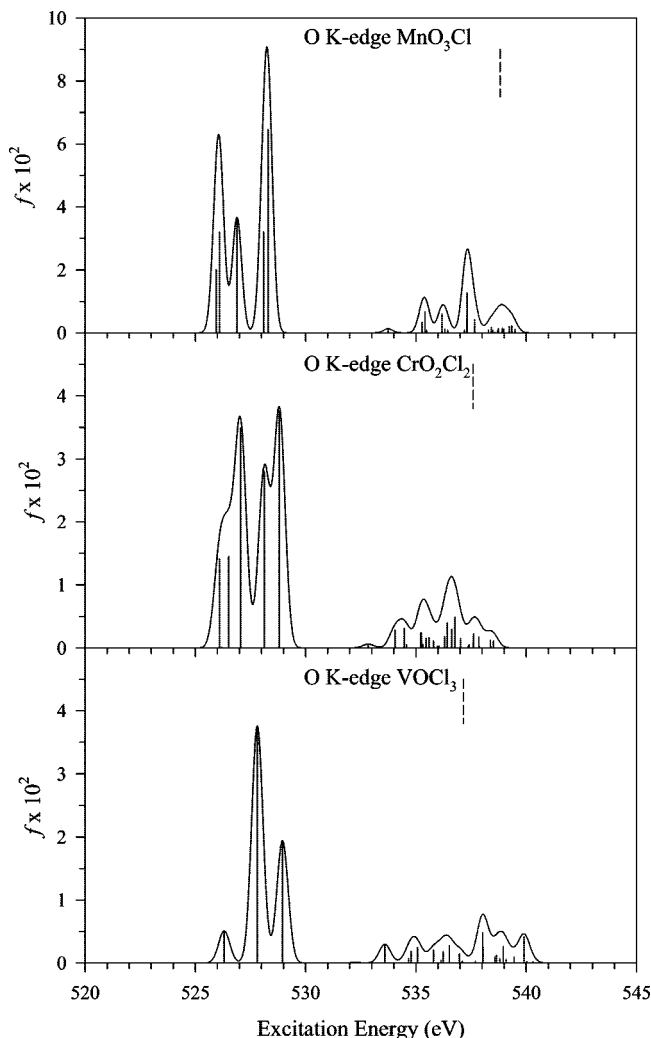


Figure 6. O K-edge two-component ZORA TDDFT spectra of MnO_3Cl , CrO_2Cl_2 , and VOCl_3 . Vertical dashed lines: calculated O 1s ionization limit. Convolved profiles are obtained with a Gaussian broadening of 0.6 eV of full width at half-maximum.

to lower lying $2p \rightarrow 10e$ transitions. Their closeness to peak A as well as their low intensity (the total f value summed over the lines is 0.065) does not allow them to be distinguished as a separate peak in the calculated spectrum. A significant configuration mixing characterizes some of the final states in this region. The increase of the Mn 3d component in the upper virtual level of the valence manifold is responsible for the higher intensity of peak C, following the trend observed also in the previous molecules. The D and E peaks of the higher energy feature are associated with virtual valence transitions from the $4e_{1/2}$ spinor, and therefore represent the $2p_{1/2}$ SO partner states of the A, A', and B peaks of the L_3 band. In this energy range also Rydberg transitions converging to the L_3 -edge are present with lower intensity. Peak F consists of a large number of lines among which the most intense is associated with the $4e_{1/2} \rightarrow 11e$ transition, which is therefore the SO partner state of the transition of the C peak. At the higher energy side of peak F the small features labeled G, H, and I are associated to transitions from the $2p_{3/2}$ core hole state into virtual levels above the L_3 ionization threshold, while the L feature is contributed by the first Rydberg excitations from the $2p_{1/2}$ core orbital. The details of the excitations contributing to G–L features can be found in Table S3 in the Supporting Information.

We can now compare the 2p metal spectra of the oxochlorides, which are aligned in Figure 4 according to the

calculated binding energy of the $2p_{3/2}$ ionization threshold. All the spectra are characterized by two main features below the L_2 -edge, previously indicated as L_3 and L_2 bands. The energy separation between these two bands increases from the V 2p to the Mn 2p spectrum, in line with the trend followed by the 2p SO splitting (calculated values are 7.2 eV for V 2p, 8.7 eV for Cr 2p, and 9.8 eV for Mn 2p). The spectra clearly show the significant deviations from the statistical intensity ratio of 2:1 for the L_3 and L_2 bands, which is also the behavior observed in the experimental 2p spectra of the pure 3d transition metals.¹ The main origin of this effect has been ascribed to the strong correlation due to the coupling of the 2p core wave function and the 3d wave function.⁴ The calculations also show that 3d spin–orbit coupling of the empty 3d orbitals is very small, around 0.02 eV for both VOCl_3 and MnO_3Cl , so it is not expected to influence significantly the distribution of intensity between the L_3 - and L_2 -edges. The calculated intensity of the lower L_3 band is almost constant across the series, but it is apparent that its shape changes along the series reflecting the molecular field and covalency effects. The C_{3v} symmetry of the compounds VOCl_3 and MnO_3Cl splits the 3d shell into three virtual valence levels (two of e and one of a_1 symmetry) giving rise to the three-peaked structure of the L_3 band in the V 2p and Mn 2p spectra; the different metal–ligand interaction, namely the increase of covalent interaction when halogens are substituted by oxygen atoms from V to Mn, also contributes to the different intensity distribution among the three peaks of the L_3 band. In the Cr compound the decrease of symmetry to C_{2v} causes a further loss of degeneracy of the 3d shell, which splits into five virtual valence levels that give rise to four peaks in the L_3 band. The shape of the L_2 bands resembles closely that of the L_3 bands, although the number and the nature of transitions contributing to them is significantly different, because of the presence of Rydberg excitations converging to the L_3 -edge which overlap with the L_2 valence transitions. The calculated valence transitions starting from the $2p_{1/2}$ core level are in any case less intense than the corresponding L_3 excitations.

4.2. O K-Edge Spectra. The O K-edge excitations originate from the 1s orbitals of the oxygen ligand and for the dipole selection rules only transitions to the 2p and np oxygen components of the final MOs can acquire intensity. Although the transitions involve oxygen MOs, the spectral structures observed at the O K-edge are determined by the electronic structure around the 3d transition metal. In fact the covalent metal–oxygen interaction reduces the O 2p ligand component in the occupied MOs introducing oxygen 2p character in the valence unoccupied MOs of mainly 3d metal character (see Scheme 1). Therefore the oscillator strength of the O 1s transitions can provide a direct probe of the covalency of the ligand–metal bond.

The experimental and theoretical O K-edge spectra of VOCl_3 and CrO_2Cl_2 are compared in Figure 5 while Figure 6 shows the calculated spectra of all three oxochlorides. Table 4 reports the results relative to the O 1s valence excited states only. All the O 1s theoretical spectra exhibit two distinct regions: the valence region characterized by an intense structure which is attributed to oxygen 2p contributions in states with predominant 3d metal character and a higher energy region with less intense features attributed to oxygen np contributions to the high energy excited states (Rydberg transitions).

As we can see in Figure 6, the calculated oscillator strengths of the valence transitions increase from V to Mn with the number of oxygen atoms in the molecules; the same trend is, however, conserved also if we consider the intensity values

TABLE 4: Experimental and Calculated Valence Excitation Energies (eV) and Oscillator Strengths f of the O K Spectra of VOCl_3 , CrO_2Cl_2 , and MnO_3Cl ^a

VOCl_3					
exptl					
E (eV)	10^2f ($\pm 10\%$)		E (eV)	10^2f	final state/dominant character
(530.03(1))	1.2		(526.31)	0.508	13e/3d V (60%), 3p Cl (23%), 2p O (5%)
1.03(1)	3.1		1.50	3.762	14e/3d V (58%), 2p O (18%), 3p Cl (17%)
2.03(1)	2.0		2.64	1.943	16a ₁ /3d V (54%), 2p O (32%), 3p Cl (11%)
4.7(1)	1.8				
6.0(1)	5.6				
CrO_2Cl_2					
exptl					
E (eV)	10^2f ($\pm 20\%$)		E (eV)	10^2f	final state/dominant character
(528.61 (3))	0.3	A	(526.10)	1.414	17a ₁ /3d Cr (45%), 2p O (20%), 3p Cl (18%)
0.25 (3)	1.5		0.42	1.451	4a ₂ /3d Cr (46%), 2p O (36%), 3p Cl (5%)
0.51 (8)	1.7	B	0.95	3.490	11b ₁ /3d Cr (45%), 3p Cl (26%), 2p O (18%)
1.94 (2)	1.3		2.02	2.794	18a ₁ /3d Cr (45%), 2p O (33%), 3p Cl (12%)
2.64 (2)	1.7		2.71	3.756	9b ₂ /3d Cr (44%), 2p O (43%), 3p Cl (4%)
MnO_3Cl					
E (eV)					final state/dominant character
(525.95)			2.015		10e/3d Mn (41%), 2p O (43%), 3p Cl (5%)
0.15			4.619		10e
0.94			3.650		15a ₁ /3d Mn (45%), 2p O (33%), 3p Cl (23%)
2.15			3.211		11e/3d Mn (42%), 2p O (55%), 3p Cl (1%)
2.35			6.760		11e

^a Absolute excitation energies are given for the first transition; relative excitation energies are reported for the following transitions.

normalized to a single O atom ($f = 6.22$, 6.45 , and 6.75 for VOCl_3 , CrO_2Cl_2 , and MnO_3Cl , respectively). This result correctly reflects the increase of covalency from the V to the Mn compound. Figure 6 also shows that the oxygen K-edge is sensitive to changes in the local transition metal geometry as a consequence of the strong 3d metal–2p oxygen hybridization. In fact the structure of the O K-edge absorption reflects the molecular symmetry set up by the oxygen ligands surrounding the central metal atom and the consequent split of the 3d metal states. In our computational scheme the transitions starting from the O 1s core orbital are toward the same virtual MOs involved in the 2p metal spectra therefore the energy position of the lines is conserved while the intensity now is proportional to the weight of oxygen p content in the mainly 3d virtual MOs (3d band). Therefore some correspondence between the O K-edge and the L metal edge can be observed for these molecules.

The O 1s valence structure of VOCl_3 reflects the C_{3v} molecular symmetry that splits the 3d metal states into the three virtual valence levels 13e (LUMO), 14e, and 16a₁. The low intensity found for the transition to the LUMO reflects the dominant V 3d and Cl 3p character of the orbital with only a small participation from the O ligand (see also Table 4). A stronger O 2p contribution is instead present in the following valence virtual states (14e and 16a₁), at the expense of Cl ligand participation. The comparison with experiment is quite satisfactory (see Figure 5a) for the energy separation between the three valence peaks; a discrepancy is apparent in the distribution of intensity between the first two peaks: the calculated one is lower than in the measurement for the first peak and higher for the second peak. A possible origin of this disagreement is the presence of the V 2p_{1/2} edge in the energy region of the O 1s transitions (532.55 eV in the calculation), so that some V 2p_{1/2} transitions could contribute to the intensity of the first experimental peak. The Rydberg transitions of the calculated O 1s excitation spectrum are well separated in energy

from the valence structure and have quite low intensity; the experimental measurement does not show resolved structure at higher energy probably due to the difficulty to detect broad low-intensity features on the intensity scale of the valence transitions, and to the coexistence in the same energy range of Rydberg transitions both from V 2p and O 1s based excitations (cf. Figure 1), resulting in two weak and diffuse structures peaked at 4.7 and 6.0 eV.

The valence structure of the theoretical O 1s spectrum of CrO_2Cl_2 consists of five lines corresponding to transitions to the virtual valence MOs of Cr 3d main character, split into five levels by the C_{2v} symmetry, among which the O 2p component is distributed. The first three transitions give rise to a quite broad structure: a lower energy shoulder is due to the 17a₁ and 4a₂ transitions with similar intensity while the main peak corresponds to the 11b₁ transition. The second two-peaked structure is associated with the 18a₁ and 9b₂ transitions, respectively. The intensity trend reflects the increase of the O 2p content on going toward the upper valence levels, as observed also for VOCl_3 . The stronger metal–oxygen bonding gives rise to higher lying antibonding orbitals. The experimental spectrum (Figure 5b) shows two peaks, the second slightly less intense than the first and much broader, possibly because of extensive vibrational excitation. The agreement with the theoretical results is good for the energy separation of the two peaks, but their intensity ratio is apparently reversed. Actually the intensity ratio of the two structures, which we indicate by A and B, is $A/B = 6.5/6.7 = 0.97$ in the theoretical calculations, and is rather well reproduced in the experimental data ($3.5/3 = 1.17$). On the contrary, the agreement between the calculated and the measured oscillator strength is rather poor. Considering the fact that experimental data are not correctly reproducing the expected increase in the O 1s cross section, we suspect that the instabilities of the photon beam mentioned above could have been particu-

larly severe during the acquisition of these data resulting in worse photon resolution than we estimated, and thus increasing the error in the derived oscillator strength. The calculated intensity of the Rydberg transitions is not negligible as for the previous molecule; however, no experimental structure is clearly resolved at higher energy showing only a diffuse structure centered around 542 eV.

The O 1s valence structure calculated for MnO_3Cl is again characterized by three peaks, as expected on the basis of the splitting of the Mn 3d orbitals in the C_{3v} symmetry. The first and third valence peaks correspond to the transitions from the $5a_1$ and $2e$ O 1s orbitals toward 10e and 11e final MOs, as shown in Table 4, and each of them consists of two components. These derive from the combination of $5a_1 \rightarrow 10e$ and $2e \rightarrow 10e$ transitions for the first peak and $5a_1 \rightarrow 11e$ and $2e \rightarrow 11e$ transitions for the third peak in the E final symmetry of the total wave function, among which the intensity is redistributed. The second peak corresponds to the $5a_1 \rightarrow 15a_1$ transition, while the corresponding $2e \rightarrow 15a_1$ transition acquires negligible intensity. The oscillator strength follows the same trend observed for the previous spectra, with an increase of the O 2p content in the upper virtual valence levels. The Rydberg structure appears shifted to higher energy with respect to the other two oxychlorides, namely more separated from the valence structure.

5. Conclusions

Excellent agreement between theoretical and experimental 2p metal photoabsorption spectra proves the capability of the relativistic ZORA TDDFT approach to describe the complex effects involved in the spectroscopy of degenerate core holes of 3d transition metal compounds. A theoretical description of the metal 2p edge must include SO as well as the treatment of the interaction between the 2p-hole and the 3d electrons to give a reliable simulation of the experimental spectra. The large SO coupling present in these molecules gives rise to a wide L_3/L_2 energy gap with an intensity distribution between the two series of excited states that deviates from the statistical intensity ratio of 2:1 for the L_3 and L_2 bands. The variations of the spectral features at the metal L_3 edge are mostly associated with the changing of the molecular symmetry and ligand interaction strength around the central metal atom; the spectral features of the L_2 band are less resolved in the experiment and its shape is also influenced by the presence of Rydberg transitions converging to the L_3 edge.

Significant intensity characterizes the O 1s valence transitions indicating the strong participation of the O 2p component to the virtual valence levels of mainly 3d metal character. The calculations show that this intensity can be related to the degree of covalency, which increases along the series V—Cr—Mn. Comparison with experimental spectra allows the assignment of the spectral features, although some deficiencies are apparent in the quantitative reproduction of experimental intensities.

Acknowledgment. This work has been supported by grants from MIUR (Programmi di Ricerca di Interesse Nazionale PRIN 2006) of Italy.

Supporting Information Available: The complete tables of metal $L_{2,3}$ spectra of VOCl_3 , CrO_2Cl_2 , and MnO_3Cl , with excitation energies and oscillator strengths f up to the L_2

ionization threshold. This material is available free of charge via the Internet at <http://pubs.acs.org>.

References and Notes

- (1) Fink, J.; Müller-Heinzerling, Th.; Scheerer, B.; Speier, W.; Hillbrecht, F. U.; Fuggle, J. C.; Zaanen, J.; Sawatzky, G. A. *Phys. Rev. B* **1985**, *32*, 4899.
- (2) Zaanen, J.; Sawatzky, G. A.; Fink, J.; Speier, W.; Fuggle, J. C. *Phys. Rev. B* **1985**, *32*, 4905.
- (3) de Groot, F. M. F.; Fuggle, J. C.; Thole, B. T.; Sawatzky, G. A. *Phys. Rev. B* **1990**, *42*, 5459.
- (4) de Groot, F. M. F.; Hu, Z. W.; Lopez, M. F.; Kaindl, G.; Guillot, F.; Tronc, M. J. *Chem. Phys.* **1994**, *101*, 6570.
- (5) Ankudinov, A. L.; Ravel, B.; Rehr, J. J.; Conradson, S. D. *Phys. Rev. B* **1998**, *58*, 7565.
- (6) Hebert, C. *Micron* **2007**, *38*, 12.
- (7) Baerends, E. J.; Ellis, D. E.; Ros, P. *Chem. Phys.* **1973**, *2*, 41.
- (8) Nesvizhskii, A. I.; Rehr, J. J. *J. Synchrotron Radiat.* **1999**, *6*, 315.
- (9) Marques, M. A. L.; Gross, E. K. U. *Annu. Rev. Phys. Chem.* **2004**, *55*, 427.
- (10) Wang, F.; Ziegler, T.; van Lenthe, E.; van Gisberger, S.; Baerends, E. J. *J. Chem. Phys.* **2005**, *122*, 204103.
- (11) Fronzoni, G.; Stener, M.; Decleva, P.; Wang, F.; Ziegler, T.; van Lenthe, E.; Baerends, E. J. *Chem. Phys. Lett.* **2005**, *416*, 56.
- (12) Fronzoni, G.; De Francesco, R.; Stener, M.; Decleva, P. *J. Chem. Phys.* **2007**, *126*, 134308.
- (13) Zangwill, A.; Soven, P. *Phys. Rev. A* **1980**, *21*, 1561. Levine, Z. H.; Soven, P. *Phys. Rev. A* **1984**, *29*, 625.
- (14) Schmittalla, J.; Ebert, H. *Phys. Rev. Lett.* **1998**, *80*, 4586.
- (15) Decleva, P.; Fronzoni, G.; Lisini, A.; Stener, M. *Chem. Phys.* **1994**, *186*, 1. Stener, M.; de Simone, M.; Fronzoni, G. *Chem. Phys. Lett.* **2003**, *373*, 115.
- (16) Martins, M.; Godehusen, K.; Richter, T.; Wernet, P.; Zimmermann, P. J. *Phys. B: At. Mol. Opt. Phys.* **2006**, *39*, R79, and reference cited therein.
- (17) Richter, T.; Godehusen, K.; Martins, M.; Wolff, T.; Zimmermann, P. *Phys. Rev. Lett.* **2004**, *93*, 023002.
- (18) Fronzoni, G.; Coreno, M.; de Simone, M.; Franceschi, P.; Furlani, C.; Furlan, S.; Prince, K. C.; Stener, M.; Decleva, P. *Phys. Chem. Chem. Phys.* **2003**, *5*, 2758.
- (19) Hocking, R. K.; Wasinger, E. C.; Yan, Y.-L.; de Groot, F. M. F.; Walker, F. A.; Hodgson, K. O.; Hedman, B.; Solomon, E. I. *J. Am. Chem. Soc.* **2007**, *129*, 113.
- (20) Hocking, R. K.; Wasinger, E. C.; Yan, Y.-L.; de Groot, F. M. F.; Walker, F. A.; Hodgson, K. O.; Hedman, B.; Solomon, E. I. *J. Am. Chem. Soc.* **2006**, *128*, 10442.
- (21) Hitchcock, A. P.; Wen, A. T.; Rühl, E. *Chem. Phys.* **1990**, *147*, 51. Wen, A. T.; Hitchcock, A. P. *Can. J. Chem.* **1992**, *71*, 100.
- (22) Mazza, T.; Piseri, P.; Bongiorno, G.; Ravagnan, L.; Amati, M.; Devetta, M.; Lenardi, C.; Coreno, M.; de Simone, M.; Milani, P. *Appl. Phys. A: Mater. Sci. Process.* **2008**, *92*, 463. Piseri, P.; Mazza, T.; Bongiorno, G.; Devetta, M.; Coreno, M.; Milani, P. *J. Electron Spectrosc. Relat. Phenom.*, In press.
- (23) Casarin, M.; Finetti, P.; Vittadini, A.; Wang, F.; Ziegler, T. *J. Phys. Chem. A* **2007**, *111*, 5270.
- (24) Casida, M. E. In *Recent Advances in Density-Functional Methods*; Chong, D. P., Ed.; World Scientific: Singapore, 1995; p 155.
- (25) Davidson, E. R. *J. Comput. Phys.* **1975**, *17*, 87.
- (26) van Lenthe, E.; Baerends, E. J. *J. Comput. Chem.* **2003**, *24*, 1142.
- (27) van Leeuwen, R.; Baerends, E. J. *Phys. Rev. A* **1994**, *49*, 2421.
- (28) Jasinski, J. P.; Holt, S. L.; Wood, J. H.; Moskowitz, J. W. *J. Chem. Phys.* **1975**, *63*, 1429.
- (29) Blyth, R. R.; Delaunay, R.; Zitnik, M.; Krempasky, J.; Krempaska, R.; Slesak, J.; Prince, K. C.; Richter, R.; Vondracek, M.; Camilloni, R.; Avaldi, L.; Coreno, M.; Stefani, G.; Furlani, C.; de Simone, M.; Stranges, S.; Adam, M.-Y. *J. Electron Spectrosc. Relat. Phenom.* **1999**, *101*–103, 959.
- (30) Domcke, M.; Mandel, T.; Puschmann, A.; Xue, C.; Shirley, D. A.; Kaindl, G.; Petersen, H.; Kurske, P. *Rev. Sci. Instrum.* **1992**, *63*, 80.
- (31) de Simone, M.; Coreno, M.; Alagia, M.; Richter, R.; Prince, K. J. *Phys. B: At. Mol. Opt. Phys.* **2002**, *35*, 61.
- (32) Chan, W. F.; Cooper, G.; Brion, C. E. *Phys. Rev. A* **1991**, *44*, 186.
- (33) Jolly, W. L.; Avanzino, S. C.; Lazarus, M. S.; Perry, W. B.; Riezt, R. R.; Shaaf, T. H. *Inorg. Chem.* **1975**, *14*, 1595.
- (34) de Groot, F. M. F.; Fuggle, J. C.; Thole, B. T.; Sawatzky, G. A. *Phys. Rev. B* **1990**, *41*, 928.
- (35) de Groot, F. M. F. *Coord. Chem. Rev.* **2005**, *249*, 31.